Dynamical theory of molecular photoionization: Electron ejection kinematics and angular distributions from molecules fixed in space

ARTICLE *in* JOURNAL OF ELECTRON SPECTROSCOPY AND RELATED PHENOMENA · MAY 2002

Impact Factor: 1.44 · DOI: 10.1016/S0368-2048(02)00014-2

3 AUTHORS, INCLUDING:

Peter Langhoff
University of California, San Diego
154 PUBLICATIONS **3,996** CITATIONS
SEE PROFILE

Julio Cesar Arce
Universidad del Valle (Colombia)
27 PUBLICATIONS **170** CITATIONS
SEE PROFILE

ELSEVIER

Journal of Electron Spectroscopy and Related Phenomena 123 (2002) 117–132

JOURNAL OF ELECTRON SPECTROSCOPY and Related Phenomena

www.elsevier.com/locate/elspec

Dynamical theory of molecular photoionization: electron ejection kinematics and angular distributions from molecules fixed in space☆

P.W. Langhoff[a,b,*], J.C. Arce[c], J.A. Sheehy[a]

[a] *Air Force Research Laboratory, AFRL/PRSP, Edwards AFB, CA 93524-7680, USA*

[b] *San Diego Supercomputer Center, University of California–San Diego, 9500 Gilman Drive, MS 0505, La Jolla, CA 92093-0505, USA*

[c] *Departamento de Quimica, Universidad del Valle, A.A. 25360 Cali, Colombia*

Received 18 December 2001; received in revised form 25 January 2002; accepted 30 January 2002

Abstract

Photoionization of molecules and other atomic aggregates fixed in space is studied from a dynamical perspective employing solutions of the time-dependent Schrödinger equation. The wave functions and associated kinematical behaviors of excited and ejected electrons are determined explicitly in short- and long-time limits, generalizing early results of Bethe for central potentials to anisotropic targets. Ehrenfest's theorem is employed to clarify the origins of the transient forces and consequent kinematical behaviors of excited and ionized K-shell electrons obtained from explicit solutions of the time-dependent Schrödinger equation, revealing hybrid classical-quantal behaviors in wave functions and expectation values of position and momentum operators. In addition to providing pedagogical insights into time-resolved aspects of these fundamental photoprocesses, and a corresponding basis for theoretical studies of dynamical target relaxation, associated photoelectron-ion correlation, and other specifically time-dependent post-collision interaction phenomena, the new development resolves technical issues associated with the irreducibly infinite degeneracy of the scattering continuum for the anisotropic potentials characteristic of polyatomic molecules. Photoionization cross sections differential in electron ejection angles are derived from the formalism for fixed-in-space molecules of arbitrary complexity which are applicable in both time-resolved and steady-state situations, and an invariant subspace of excitation and ionization functions required in computational applications of the approach is constructed employing Lanczos–Krylov sequences of L^2 vectors and previously devised Stieltjes–Akhiezer methods, without reference to or calculations of the underlying individual discrete or continuum eigenstates. Electron angular-distribution data for fixed-in-space molecules measured over the full (4π) range of emission angles for all molecular orientations are shown to be highly redundant, and to provide invariant physical information in the form of no more than three irreducible-tensor body-frame complex angular emission amplitudes at a given photon energy. These issues are illustrated with applications to ionization of fixed-in-space diatomic molecules for linear and circularly polarized incident radiation, in which cases the minimal set of molecular configurations and polarizations required to determine the invariant body-frame emission amplitudes is described in detail.

Keywords: Angular distributions; Dynamical theory; Electron ejection kinematics; Fixed-in-space molecules; Molecular photoionization

☆Work supported in part by grants from the US Air Force Office of Scientific Research and COLIENCIAS of Colombia.

*Corresponding author. Tel.: +1-858-822-3611; fax: +1-858-534-5113.

E-mail address: langhoff@drifter.sdsc.edu (P.W. Langhoff).

0368-2048/02/$ – see front matter
PII: S0368-2048(02)00014-2

1. Introduction

Photoionization of molecules and other forms of matter is a widely pervasive quantum phenomenon intimately associated with development of quantum theory [1–3], and has long been employed as a diagnostic tool in material science and related disciplines [4,5]. Recent synchrotron-radiation-based studies of the angular distributions of electrons photoejected from fixed-in-space molecules yield new insights into the nature of the photoejection process in these prototypical anisotropic materials [6–16], which provide a useful vehicle for interpreting similar phenomena in more complex nanoscale aggregates and condensed matter. Related time-resolved imaging techniques furnish insights into the dynamics of photoexcitation processes in a great variety of situations, including aspects of post-collision photoelectron–ion relaxation and correlation effects, parent-ion fragmentation processes, chemical reactions, and other specifically time-dependent phenomena [17,18].

Standard theoretical descriptions of molecular photoionization processes based on calculations of directed- and partial-wave representations of continuum eigenfunctions do not provide time-resolved information, and can become computationally inefficient when many angular-momentum waves contribute [19–27], with results generally obtained numerically from infinite l-wave expansions in the absence of simple analytical cross sectional expressions. Moreover, the irreducibly infinite degeneracy of continuum eigenstates for anisotropic potentials, and the associated arbitrariness in descriptions of final states, has long obscured the physical nature of the wave function produced by the ionization process in polyatomic molecules. It would clearly be desirable to devise analytical expressions for differential cross sections and other physical observables that can provide time-resolved descriptions of molecular ionization processes, and that facilitate identification and interpretation of the essential physical information obtained from recently reported fixed-in-space experiments.

Following an early development of Bethe [28–31], the photoejection process is treated here as a dynamical or initial value problem employing solutions of the time-dependent Schrödinger equation. This approach not only provides time-resolved information, but also avoids particular choices of scattering boundary conditions, giving considerably more flexibility in representations of ejection amplitudes than is possible in the customary static theory [19–27]. Although explicitly time-dependent perspectives are commonly employed in studies of the interactions of atoms with intense radiation fields [32], and of molecular photodissociation processes [33], little attention appears to have been directed at similar descriptions of the explicit spatio-temporal development of molecular photoionization.

In the present report, the dynamics of electron photoejection in anisotropic potentials is quantified, aspects of the kinematical behaviors of excited and ejected electrons are clarified on a common basis, the Hilbert subspace accessed by time evolution of the wave function in the presence of an electromagnetic perturbation is characterized, and explicit cross-sectional expressions valid in time-resolved situations are provided. These results generalize to anisotropic potentials and elaborate upon the aforementioned early studies of Bethe [28], who first demonstrated how solutions of the time-dependent Schrödinger equation for photoejection in central potentials evolve naturally from initial bound states into outgoing waves, justifying the use of stationary scattering eigenstates that satisfy incoming radial-wave boundary conditions in the standard time-independent differential cross-sectional expressions [29].

In Section 2, the short- and long-time limits of solutions of the time-dependent Schrödinger equation are derived in analytical forms for anisotropic potentials, and calculations are reported of time-dependent wave functions and of the relevant dynamical information for photoexcitation and photoejection which span these limits. The Hilbert subspace in which the wave function evolves is revealed, and methods are described for efficient construction of many-electron non-degenerate prepared states which resolve the irreducibly infinite degeneracy of the scattering continuum for anisotropic potentials [34–37]. Hybrid classical-quantal dynamical behaviors of the wave functions and expectation values of electron position and momentum operators for discrete transitions and continuum photoejection are described on basis of computational studies of such motions in Coulombic potentials to illustrate the

predicted behaviors. Ehrenfest's Theorem is seen to clarify the origins of the transient forces responsible for electron excitation and ejection, of the different kinematical behaviors obtained from below- or above-threshold photons, and of the associated time scales of the excitation and ejection processes.

In Section 3, differential photoionization cross sections for fixed-in-space molecules and other atomic aggregates are obtained from spatially and temporally asymptotic probability amplitudes, which are given by (complex) outgoing radial waves modulated in their angular variations by the potential field experienced by the departing electrons. All dependences of the differential cross section upon the orientation of the molecule in the laboratory frame are given in analytical forms for the general case of elliptically polarized monochromatic radiation, aiding in interpretations of fixed-in-space photoionization measurements without reliance on detailed wave function calculations. Explicit expressions are provided for differential photoionization cross sections in anisotropic potentials in terms of previously defined non-degenerate Stieltjes–Akheizer states of irreducible symmetry which can be constructed with L^2 methods [35–37]. Application are provided for diatomic molecules in linear and circularly polarized radiation fields, in which cases only two real non-negative amplitudes and one relative phase are required to determine the differential cross section for all possible molecular orientations and states of polarization of the incident monochromatic photons.

Concluding remarks provided in Section 4 summarize the material reported here, and also touch upon additional experimental studies that are related to recently reported fixed-in-space molecular photoionization measurements.

2. Schrödinger dynamics

Solutions of the time-dependent Schrödinger equation:

$$\left(\hat{H}^{(0)}(\boldsymbol{r}) + \hat{H}^{(1)}(\boldsymbol{r}, t) - i\hbar\frac{\partial}{\partial t}\right)\Psi(\boldsymbol{r}, t) = 0 \qquad (1)$$

determine the dynamical outcome of an event when the value of the wave function $\Psi(\mathrm{r},\ t = 0)$ is specified at some initial time ($t = 0$). The required initial condition is provided in the case of photoexcitation or ionization by the field-free wave function $\Psi^{(0)}(\boldsymbol{r},\ t) = \Phi_g(\boldsymbol{r})\,\mathrm{e}^{-iE_g t/\hbar}$, where $\Phi_g(\boldsymbol{r})$ is the ground vibronic eigenstate in the absence of rotation. The Hamiltonian operator $\hat{H}^{(0)}(\boldsymbol{r})$ in this case accordingly describes a many-electron molecule or other finite atomic aggregate fixed in space, with the effects of incident radiation included in the familiar semi-classical perturbation operator for monochromatic radiation [2,3]

$$\hat{H}^{(1)}(\boldsymbol{r}, t) = \frac{eA_0}{mc}(\hat{\boldsymbol{\epsilon}}\cdot\boldsymbol{p})\,e^{i\boldsymbol{k}_p\cdot\boldsymbol{r}}\cos(\omega t). \qquad (2)$$

Here, $\boldsymbol{k}_p$ is the photon propagation vector, A_0 is the magnitude of the vector potential for monochromatic photons of circular frequency ω which are linearly polarized in the direction of the unit vector $\hat{\boldsymbol{\epsilon}}$, $\boldsymbol{r}$ and $\boldsymbol{p}$ refer to the position and momentum operators of the target electrons, and suitable switching on of the electromagnetic perturbation is implied. In the familiar uniform-electric-field approximation, the photon propagation vector in Eq. (2) is set to zero ($\boldsymbol{k}_p \to 0$), the exponential phase factor is unity, and solutions of Eq. (1) are constructed up to first order in the radiation field $\left(\Psi(\boldsymbol{r}, t) = \Psi^{(0)}(\boldsymbol{r}, t) + \Psi^{(1)}(\boldsymbol{r}, t) + \cdots\right)$ [38].

In contrast to conventional stationary-state treatments of molecular photoionization, in which cases cross sections are devised in terms of continuum eigenfunctions [39], Eq. (1) can provide time-resolved information, as well as results in long-time limits that are equivalent or supplemental to the predictions of the stationary-state development [19–27]. Specifically, questions related to choices of scattering-wave boundary conditions which arise in the static approach for anisotropic potentials, consequent of the irreducibly infinite degeneracy of continuum eigenfunctions in this case, are avoided entirely in obtaining solutions of Eq. (1), and alternative methods for calculating differential cross sections can be devised from the time-dependent development in the limit $t \to \infty$.

Although the eigenstates of the molecular Hamiltonian $\hat{H}^{(0)}(\boldsymbol{r})$ are not necessarily required in constructing solutions of Eq. (1), it is useful *for purposes of analysis* to employ them in writing the familiar wave function first order in A_0 in the form of the spectral expansion

$$\Psi^{(1)}(\boldsymbol{r},t)=\frac{eA_0}{2mc}\int_{-\infty}^{+\infty}\mathrm{d}E\ \mathrm{e}^{-iEt/\hbar}\,\mu(E)\,\Phi_E(\boldsymbol{r})$$
$$\times\left\{\frac{\left[\cos\left(\omega_{E_g}\pm\omega\right)t-1\right]}{\hbar\left(\omega_{E_g}\pm\omega\right)}+i\frac{\sin\left(\omega_{E_g}\pm\omega\right)t}{\hbar\left(\omega_{E_g}\pm\omega\right)}\right\}. \quad (3)$$

Here, the spectral integral over the energy variable E implies also summation over bound-state contributions ($E=E_n$) to the first-order wave function, the molecular transition moments $\mu(E)$ and spectral eigenstates $\Phi_E(\boldsymbol{r})$ are defined immediately below, $\omega_{E_g}=(E-E_g)/\hbar$ is the circular transition frequency between the continuum or discrete state at energy E and the ground state of energy E_g, the notation $\pm$ implies a sum over the two real and imaginary terms in the brackets, and step-function switching at $t=0$ has been employed [38].

2.1. Interaction-prepared eigenstates

The spectral eigenstates employed in Eq. (3) are written in the prepared-state form [34]

$$\Phi_E(\boldsymbol{r})=\frac{\sum_{\gamma,\alpha}\Phi_E^{(\gamma,\alpha)}(\boldsymbol{r})\langle\Phi_E^{(\gamma,\alpha)}|\hat{\boldsymbol{\epsilon}}\cdot\boldsymbol{p}|\Phi_{E_g}\rangle}{\left\{\sum_{\gamma,\alpha}|\langle\Phi_E^{(\gamma,\alpha)}|\hat{\boldsymbol{\epsilon}}\cdot\boldsymbol{p}|\Phi_{E_g}\rangle|^2\right\}^{1/2}}, \quad (4)$$

and the corresponding electric dipole transition moments are

$$\mu(E)=\langle\Phi_E|\hat{\boldsymbol{\epsilon}}\cdot\boldsymbol{p}|\Phi_{E_g}\rangle$$
$$=\frac{\sum_{\gamma,\alpha}|\langle\Phi_E^{(\gamma,\alpha)}|\hat{\boldsymbol{\epsilon}}\cdot\boldsymbol{p}|\Phi_{E_g}\rangle|^2}{\left\{\sum_{\gamma,\alpha}|\langle\Phi_E^{(\gamma,\alpha)}|\hat{\boldsymbol{\epsilon}}\cdot\boldsymbol{p}|\Phi_{E_g}\rangle|^2\right\}^{1/2}}, \quad (5)$$

where the last equality in Eq. (5) follows from use of Eq. (4). Here, $\Phi_E^{(\gamma,\alpha)}(\boldsymbol{r})$ are the vibronic spectral eigenstates of the Hamiltonian operator $\hat{H}^{(0)}(\boldsymbol{r})$, where the label γ can be chosen to represent any of the point-group symmetries of the fixed molecule for the unity-normalized bound states, with α in this case enumerating the degenerate states within an individual symmetry designation. In the continuum of molecular eigenstates, which are delta-function normalized on the energy scale and generally infinitely degenerate at any energy E [39], common choices for the labels γ, α include asymptotic ($\boldsymbol{r}\to\infty$) angular momentum values (l, m), the direction angles of the ejected electron momentum ($\hbar\boldsymbol{k}_e$), and the so-called eigenchannel labels [39–42], which correspond closely to the symmetry labels employed in the discrete spectral region [36]. When γ specifies a particular eigenchannel symmetry, α is required to enumerate the infinity of eigenstates at energy E within this symmetry. Since the sum over degenerate eigenstates in Eq. (4) forms a projector at energy E, the choice of particular eigenstates employed in its construction is arbitrary, and the resulting prepared states are invariant to this choice. Additional quantum labels generally required to enumerate many-electron molecular eigenstates uniquely are suppressed here for notational clarity.

The non-degenerate spectral functions of Eq. (4) are recognized as the prepared states of Fano and Cooper [34], which comprise a proper (invariant) subspace of the full Hilbert space spanned by the discrete states and the degenerate continuum eigenstates of $\hat{H}^{(0)}(\boldsymbol{r})$. This particular combination of molecular eigenstates clearly arises as a matter of course in Eqs. (3) and (4) employing any of the forms of molecular eigenstates indicated above, rather than as a consequence of some arbitrary choice or convention. This observation is further clarified by substituting Eqs. (4) and (5) into Eq. (3), demonstrating explicitly that $\Phi_E(\boldsymbol{r})$ is simply a convenient symbol for the generally infinite combination of degenerate eigenstates having energy E required in constructing solutions of the time-dependent Schrödinger equation. It should be noted that the prepared states of Eq. (4) refer to the N-electron target of interest, and so formally include all ionic channel interactions and corresponding many-electron relaxation and correlation effects associated with the ionization process.

2.2. Limiting behaviors

In the short time limit $t\to 0^+$, Eq. (3) is seen to take the form

$$\Psi^{(1)}(\boldsymbol{r},t)\to\frac{eA_0}{2mc}(it/\hbar)\int_{-\infty}^{+\infty}\mathrm{d}E\ \mu(E)\,\Phi_E(\boldsymbol{r})$$
$$=\frac{eA_0}{2mc}(it/\hbar)(\hat{\boldsymbol{\epsilon}}\cdot\boldsymbol{p})\,\Phi_g(\boldsymbol{r}), \quad (6)$$

employing closure in the last expression. Eq. (6) demonstrates that the function $\Psi^{(1)}(\boldsymbol{r}, t)$, although vanishing in the short-time limit, has as its initial spatial form the so-called E_1 test function associated with electromagnetic radiation in the dipole approximation, involving the indicated product of the dipole perturbation operator $(\hat{\boldsymbol{\epsilon}} \cdot \boldsymbol{p})$ and the initial eigenstate $\Phi_g(\boldsymbol{r})$ of the molecule [34–37]. In the course of time $(t > 0)$, this initial state evolves in the interaction-prepared subspace of nondegenerate eigenstates defined in Eq. (4), in accordance with Eqs. (1)–(3).

Long-time limiting solutions appropriate for the monochromatic excitation and ionization cases of interest here are obtained from Eq. (3) by neglecting the anti-resonance terms corresponding to the + signs appearing there and setting $t \to \infty$. In the case of a discrete transition, the final-state energy is found to satisfy $E_n = E_g + \hbar\omega$, where E_n is a bound excited state eigenvalue $(E_n < 0)$, and the wave function in the $t \to \infty$ limit takes the form

$$\Psi^{(1)}(\boldsymbol{r}, t) \to \frac{eA_0}{2mc}\{(it/\hbar)\, e^{-iE_n t/\hbar}\}\, \mu(E_n)\, \Phi_{E_n}(\boldsymbol{r}). \qquad (7)$$

The state $\Phi_{E_n}(\boldsymbol{r})$, which generally corresponds to a single bound state or to a number of degenerate bound eigenstates of irreducible point-group symmetry, has been selected by the imaginary energy-conserving delta-function-like term in the bracket in Eq. (3), giving rise to the resonance energy condition, with the associated real principal-value-like term also appearing there not contributing in the discrete spectral region. Evidently, the wave function of Eq. (7) diverges linearly in the limit $t \to \infty$ and takes on the spatial form of the bound states appropriate to the discrete spectral energy selected by the excitation process. This observation forms the basis for calculations of bound eigenstates employing various time-dependent approaches reported in the literature [31].

In the case of photoionization, both real and imaginary terms in the brackets in Eq. (3) contribute, the final-state energy satisfies $E = E_g + \hbar\omega$ in the long-time limit, and the wave function of Eq. (3) in the limits $\boldsymbol{r}_e \to \infty$ and $t \to \infty$ takes the form

$$\Psi^{(1)}(\boldsymbol{r}, t) \to \frac{eA_0}{mc}\, \mu(E)\, \hat{\Phi}_E(\hat{\boldsymbol{r}}_e) \left(\frac{m\pi}{2\hbar^2 k_e}\right)^{1/2} \left(\frac{1}{r_e}\right) \times e^{i\left\{k_e r_e + \frac{e^2 m}{k_e \hbar^2} \ln(2k_e r_e) - Et/\hbar\right\}} \otimes \Phi_\Gamma^{(N-1)}(\boldsymbol{r}_{N-1}) \qquad (8)$$

for $r_e \le (\hbar k_e/m)\, t$, but vanishes for $r_e > (\hbar k_e/m)\, t$, where $\boldsymbol{r}_e$ is the coordinate of the outgoing electron, $\hbar k_e$ is its limiting momentum value, $\Phi_\Gamma^{(N-1)}(\boldsymbol{r}_{N-1})$ is the parent-ion eigenfunction for the ionic channel of energy E_Γ, the symbol $\otimes$ refers to the usual symmetry-adapted product, and $\hat{\Phi}_E(\hat{\boldsymbol{r}}_e)$ is defined immediately below. Eq. (8) is obtained by employing the asymptotic $(\boldsymbol{r}_e \to \infty)$ forms of any of the representations of the molecular continuum eigenstates indicated above for the ionic channel E_Γ in the definition of Eq. (4), and using the expansion $k = k_e + (m/\hbar k_e)(E - E_g - \hbar\omega) + \cdots$ for the energy variation of these states through the electron wavenumber k in evaluating the integral of Eq. (3) [31].

Eq. (8) indicates that the asymptotic $(\boldsymbol{r}_e \to \infty, t \to \infty)$ form of the solution of Eq. (3) in the case of photoionization comprises an outgoing radial Coulomb wave confined to a sphere having the classical expansion radius $r_e = v_e t$, where $v_e = \hbar k_e/m$ is the classical velocity, modulated in electron emission angles $(\hat{\boldsymbol{r}}_e)$ by the normalized angular emission amplitude $\hat{\Phi}_E(\hat{\boldsymbol{r}}_e)$. Although the latter amplitude can be written explicitly in terms of scattering information in the form [42]

$$\hat{\Phi}_E(\hat{\boldsymbol{r}}_e) = \frac{1}{\mu(E)} \sum_{l,m} \left\{ Y_l^{(m)}(\hat{\boldsymbol{r}}_e)\, e^{i\delta_l^{(c)}(k_e)} \times \sum_{\gamma,\alpha} \langle \Phi_E^{(\gamma,\alpha)} | \hat{\boldsymbol{\epsilon}} \cdot \boldsymbol{p} | \Phi_{E_g} \rangle\, e^{i\delta_\gamma^{(\alpha)}(E)} U_{l,m}^{(\gamma,\alpha)}(E) \right\} \qquad (9)$$

it is convenient to employ other means in its evaluation which are more generally applicable to polyatomic molecules and other larger atomic aggregates. In Eq. (9), $\delta_l^{(c)}(k_e) = -l\pi/2 + \arg\Gamma(l + 1 + ie^2 m/k_e \hbar^2)$ are the l-wave Coulomb phase shifts [2], $\boldsymbol{U}(E)$ is the unitary matrix which diagonalizes the real symmetric standing-wave $\boldsymbol{K}(E)$ matrix constructed in the (l, m) representation, and $\delta_\gamma^{(\alpha)}(E)$ are the corresponding eigenchannel phase shifts for the ionic channel of interest [39–42].

2.3. Invariant dipole-prepared subspace

The proper E1 subspace required in constructing the prepared states of Eq. (4) can be generated directly without reference to the scattering information of Eq. (9) employing a Lanczos–Krylov

sequence of many-electron orthonormal functions $v_j(\mathbf{r})$, $j = 1, 2, \ldots$, obtained from the recursive equations [35–37]

$$\beta_j v_{j+1}(\mathbf{r}) = \left(\hat{A}(\mathbf{r}) - \alpha_j\right) v_j(\mathbf{r}) - \beta_{j-1} v_{j-1}(\mathbf{r}) \tag{10}$$

where the starting conditions $v_0(\mathbf{r}) = 0$ and $v_1(\mathbf{r}) = (\hat{\boldsymbol{\epsilon}} \cdot \boldsymbol{p})\, \Phi_g(\mathbf{r}) / \langle (\hat{\boldsymbol{\epsilon}} \cdot \boldsymbol{p})\, \Phi_g | (\hat{\boldsymbol{\epsilon}} \cdot \boldsymbol{p})\, \Phi_g \rangle^{1/2}$ are sufficient to obtain the indicated functions and the recurrence coefficients α_j and β_j employing finite-difference or finite-element spectral methods to construct solutions. The operator $\hat{A}(\mathbf{r})$ can be chosen to be the molecular Hamiltonian $\hat{H}^{(0)}(\mathbf{r})$, or some other well-behaved function of this operator. Note that the normalized start function $v_1(\mathbf{r})$ has precisely the same spatial form as the short-time limit ($t \to 0^+$) of the wave function $\Psi^{(1)}(\mathbf{r}, t)$ of Eq. (6), ensuring that the functions of Eq. (10) generate a Hilbert space that is optimally suited to represent the time-dependent wave function of Eq. (3) more generally.

Employing the basis of Eq. (10), the non-degenerate E1-prepared states of Eq. (4) are obtained as ($n \to \infty$) limits of the L^2 Stieltjes–Akhiezer vectors [35–37]

$$\Phi_E^{(n)}(\mathbf{r}) = N^{1/2}(E) \sum_{j=1}^{n} q_j(E)\, v_j(\mathbf{r}) \tag{11}$$

where the polynomials $q_j(E)$ satisfy the recurrence relation of Eq. (10) with $\hat{A}(\mathbf{r})$ replaced there by the energy factor $A(E)$, and the normalization factor $N^{1/2}(E)$ is required to provide unity normalization of the bound states and Dirac-delta-like normalization in the continuum. The functions of Eq. (11) have long been employed in calculations of the partial-channel photoionization cross sections of polyatomic molecules [36,37], with the continuum normalization obtained from the measure $N(E) = \mu^2(E) / \langle (\hat{\boldsymbol{\epsilon}} \cdot \boldsymbol{p})\, \Phi_g | (\hat{\boldsymbol{\epsilon}} \cdot \boldsymbol{p})\, \Phi_g \rangle$ in the absence of explicit spatially asymptotic forms of the Lanczos–Krylov sequence $v_j(\mathbf{r})$.

The foregoing development allows construction of the E1 subspace of Eq. (4) without prior reference to the continuum functions commonly employed in photoionization studies. Since the energy dependence of the functions of Eq. (11) is contained in the normalization factor and in the polynomials $q_j(E)$, which are obtained conveniently from the recursion of Eq. (10), evaluation of the energy integral of Eq. (3) is particularly efficient once the recurrence coefficients α_j and β_j have been determined. Specifically, employing Eq. (11), Eq. (3) takes the form

$$\Psi^{(1)}(\mathbf{r}, t) = \frac{eA_0}{2mc} \langle (\hat{\boldsymbol{\epsilon}} \cdot \boldsymbol{p})\, \Phi_g | (\hat{\boldsymbol{\epsilon}} \cdot \boldsymbol{p})\, \Phi_g \rangle^{1/2} \times \sum_{j=1}^{\infty} \tilde{q}_j(t)\, v_j(\mathbf{r}) \tag{12a}$$

with

$$\begin{aligned} \tilde{q}_j(t) &= \int_{-\infty}^{+\infty} \mathrm{d}E\, N(E)\, \mathrm{e}^{-iEt/\hbar} q_j(E) \\ &\quad \times \left\{ \frac{\left[\cos\left(\omega_{E_g} \pm \omega\right) t - 1\right]}{\hbar\left(\omega_{E_g} \pm \omega\right)} + i \frac{\sin\left(\omega_{E_g} \pm \omega\right) t}{\hbar\left(\omega_{E_g} \pm \omega\right)} \right\} \\ &\quad \to \int_{-\infty}^{+\infty} \mathrm{d}E\, N(E)\, \mathrm{e}^{-iEt/\hbar} q_j(E) \left\{ \frac{P}{E - E_g - \hbar\omega} \right. \\ &\quad \left. + i\pi\delta\left(E - E_g - \hbar\omega\right) \right\}, \end{aligned} \tag{12b}$$

where the principal-value (P) and delta-function integrals in the last line are obtained in the limit $t \to \infty$. In this way, the angular emission amplitudes of Eq. (9) are obtained from the large $\mathbf{r}_e$ limit of an expression similar to Eq. (11), with the real polynomials $q_j(E)$ there replaced by limiting ($t \to \infty$) values of the complex time-dependent amplitudes $\tilde{q}_j(t)$ of Eqs. (12). It should be noted that Eqs. (10)–(12) employ many-electron states, and so all ionic channels and associated correlation, relaxation, and related dynamical effects can be included in the development when the appropriate electronic configurations are employed in constructing solutions of Eq. (10) [37], although one-electron models can also be accommodated by the formalism when the configurations selected are limited to a single hole state.

2.4. Photoexcitation and ionization dynamics

Illustrative examples of time evolution spanning the short- and long-time analytical limits of Eqs. (6)–(8) are reported in Figs. 1 and 2, which depict one-electron radial motions appropriate for photoexcitation and ionization, respectively, in a simple central Coulombic potential. Although primary atten-

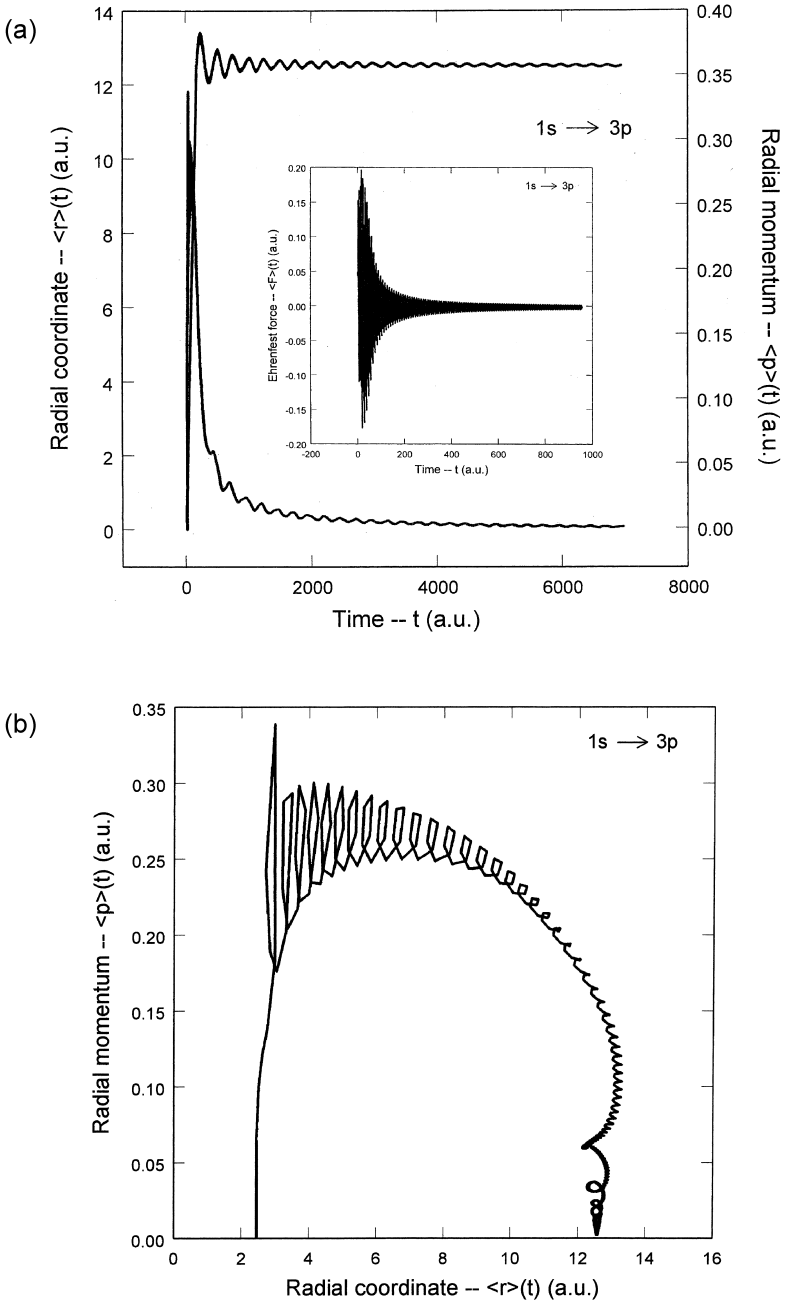

Fig. 1. (a) Photoexcitation dynamics of the 1s→3p transition in a central Coulomb potential ($\hbar\omega = 4/9$ a.u.), constructed employing Eqs. (13) and (14) and expanding-grid five-point finite differences and leapfrog propagation in solving the time-dependent Schrödinger equation [31]. The asymptotic limit $\langle r\rangle(t\to\infty)\to 25/2$ a.u. is in accord with the known 3p expectation value [2], whereas the radial momentum correctly vanishes in this limit. The insert depicts the Ehrenfest force of Eq. (13), presented on a shorter time scale than that of the position and momentum values (1 a.u. $= 2.47\times 10^{-17}$ s). (b) Trajectory of the 1s→3p transition of (a). Initial and final values of radial position are in accord with the known values ($\langle r\rangle(t\to 0^{+})\to 8/3$ a.u.; $\langle r\rangle(t\to\infty)\to 25/2$ a.u.) obtained from Eqs. (6) and (7) [2], whereas the momentum values are seen to be in accord with expectations ($\langle p\rangle(t = 0,\ \infty) = 0$). Sharp features evident in the trajectory at shorter times are consequences of the finite time-stepping interval employed in the integration procedure, and are not indicative of intrinsic kinematics [31].

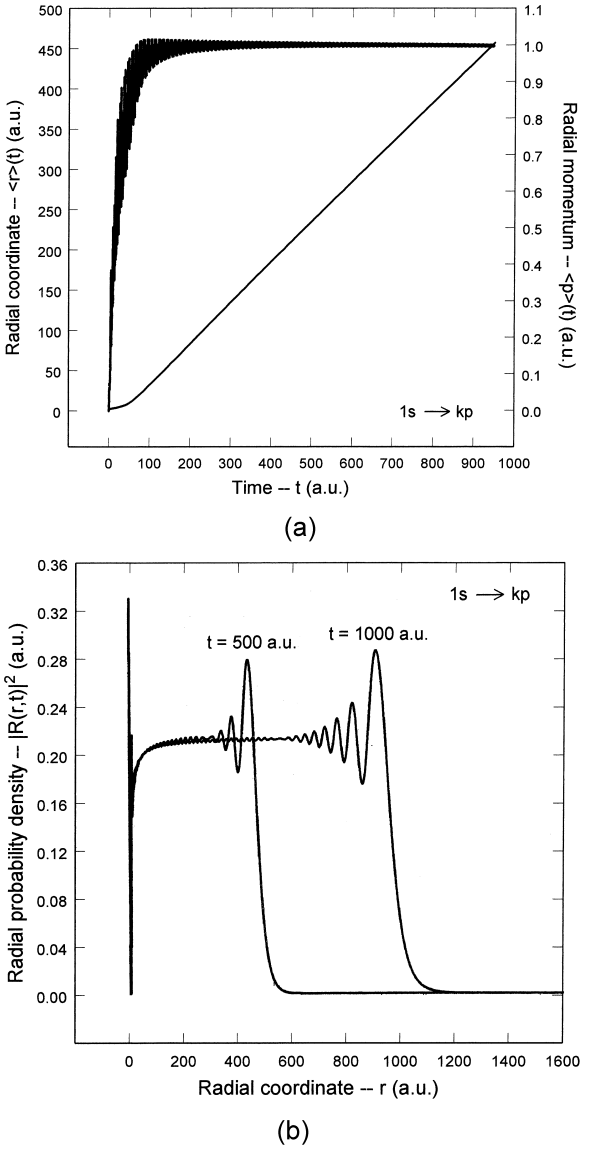

Fig. 2. (a) Photoejection dynamics of 1s→*k*p ionization in a central Coulomb potential ($\hbar\omega = 1$ a.u.), constructed as indicated in Fig. 1a and in the text. Asymptotic limits ($\langle p\rangle(t\to\infty)\to 1$ a.u.; $\langle r\rangle(t\to\infty)\to(1/2)\,v_e t$) are in accord with the analytical result for the wave function of Eq. (8). High-frequency oscillations present in the momentum values are also present in the radial position values, but are not apparent due to the large coordinate scale employed. (b) Photoejection dynamics of 1s→*k*p ionization ($\hbar\omega = 1$ a.u.), constructed as indicated in Figs. 1a and 2a, depicting the 'Bethe front' of outgoing waves of Eq. (8), obtained from direct solution of Eq. (1) for the two indicated times. The oscillations depicted at the fronts are a consequence of the well-known step ringing effect, and of the anti-resonant term in Eq. (3) neglected in deriving the analytical result of Eq. (8).

tion is focused here on the ionization process, it is of interest to contrast and compare results obtained from Eq. (3) in the two cases. Solutions of Eqs. (1)–(3) have been constructed directly employing five-point finite-difference methods on an expanding radial grid and stable leapfrog propagation of the time-dependent wave function [31]. Angular distributions and the emission amplitudes of Eq. (9) which can be obtained from the invariant subspace approach of Eqs. (10)–(12) are treated separately further below.

In Fig. 1a is shown the radial dynamics of 1s→3p Rydberg-like excitation typical of K-shell processes in light polyatomic molecules. Specifically, the insert in Fig. 1a depicts the radial Ehrenfest force

$$\langle F\rangle(t) = eE_0\cos(\omega t) + \frac{\langle\Psi^{(1)}(t)|-\nabla_r V|\Psi^{(1)}(t)\rangle}{\langle\Psi^{(1)}(t)|\Psi^{(1)}(t)\rangle}, \tag{13}$$

where the first term is the direct photoexcitation force in the dipole approximation, written in terms of the external electric field intensity $E_0 = A_0\omega/c$, and the second term is the re-scattering force associated with the atomic hole-state potential experienced by the excited electron. Note that only the dynamics carried by the first-order wave function $\Psi^{(1)}(\boldsymbol{r}, t)$ are included in Eq. (13), with contributions from the initial ground-state function neglected, in accordance with the transition case of interest here. Evidently, the force shown in the insert in Fig. 1a is highly oscillatory due to the applied field, but also includes a secular part associated with the re-scattering term in Eq. (13). Since the former averages to zero over the indicated time interval, it is the re-scattering force which is directly responsible for the resulting electron kinematical behavior, clarifying the dynamical origin of the photoexcitation process. Of course, since the form of the time-dependent wave function is determined by the externally applied field through Eq. (3), the latter is ultimately responsible for the excitation process expressed through the re-scattering term in Eq. (13).

Fig. 1a also depicts the expectation values of the radial electron position and momentum operators constructed from the calculated first-order wave function $\Psi^{(1)}(\boldsymbol{r}, t)$ and the expressions

$$\langle r\rangle(t);\ \langle p\rangle(t) = \frac{\langle\Psi^{(1)}(t)|\, r;\ -i\hbar\nabla_r|\Psi^{(1)}(t)\rangle}{\langle\Psi^{(1)}(t)|\Psi^{(1)}(t)\rangle}. \tag{14}$$

Evidently, the expectation value of radial momentum rises rapidly to a finite positive value and then falls to zero under the action of the force of Fig. 1a, whereas the corresponding expectation value of position rapidly approaches the asymptotic limit associated with completion of the 1s→3p transition ($\langle r\rangle(t\to\infty)\to 25/2$ a.u.) [2]. Note that finite values of position and momentum are given in Fig. 1a, in spite of the divergence of the first-order wave function in the limit $t\to\infty$, and that the initial value of the electron radial position ($\langle r\rangle(t\to 0^{+})\to 15/6$ a.u.) is determined by the wave function of Eq. (6), values which are unrelated to the 1s ground state [2].

In Fig. 1b is shown the associated trajectory of the transition, which is seen to exhibit a curious spiral motion to the limiting ($t\to\infty$) values of position and momentum, traversing only a small portion of the available phase space. The oscillatory behaviors of the kinematics depicted in Fig. 1a and b are consequences of the anti-resonance terms in Eq. (3), which have been neglected in deriving the analytical results of Eqs. (7) and (8). The numerical calculations performed also verify the analytical results of Eqs. (6) and (7), accordingly recovering the correct 3p radial eigenfunction in the limit $t\to\infty$ (not shown). These results, although not entirely unexpected, quantify the time-scales of the excitation process obtained from the time dynamics of Eqs. (1)–(7), and suggest that similarly insightful results can be obtained in the case of photoionization [31].

In Fig. 2 are depicted calculated results for the time evolution of 1s→*k*p electron photoejection obtained from Eqs. (1)–(8) employing an incident photon energy ($\hbar\omega = 1$ a.u.) selected to give the outgoing electron unit momentum ($\hbar k_e = 1$ a.u.). The Ehrenfest force in this case (not shown) is similar in nature but distinct in detail from that of Fig. 1a. Accordingly, the expectation values of radial momentum and position operators shown in Fig. 2a are quite different from those of Fig. 1a. Specifically, the radial momentum rises to a finite asymptotic value ($\langle p\rangle(t\to\infty)\to 1$ a.u.) in accordance with energy conservation ($E = \hbar^2 k_e^2/2m = \hbar\omega + E_g = 1/2$ a.u.), whereas the radial position increases without limit.

Consideration of the results of Fig. 2a reveals that the rate of change with time of radial position is only one-half that expected from the asymptotic momentum value. The origin of this modest failure of Ehrenfest's theorem ($\mathrm{d}\langle r\rangle(t)/\mathrm{d}t = \langle p\rangle(t)/m$) is clarified by the wave functions of Fig. 2b, which depict the 'Bethe front' predicted by the analytical result of Eq. (8). It is the *front* of the time-dependent wave function of Fig. 2b that moves with the asymptotic or classical speed, whereas the mean value of position moves with one-half this speed due to the delocalized nature of the wave function obtained, which is seen to extend from the origin to the position of the front. This hybrid classical-quantal result obtains so long as the electromagnetic perturbation of Eq. (2) is not switched off, in which event the extended wave function produced to that point is found to break off and move with the classical speed as a packet of finite length, disconnected from its atomic origin (not shown) [31]. The results of Fig. 2b demonstrate how the quantum photoionization transition rate is carried at the classically anticipated speed to a remote detector by the amplitude of the time-dependent wave function, and suggests that cross sections can be determined directly in this way from the asymptotic wave functions of Eqs. (8) and (9).

3. Photoionization cross sections

Photoionization cross sections differential in direction of outgoing electrons for molecules having a particular orientation, as specified by Euler angles ($\hat{\boldsymbol{R}} \equiv \alpha,\ \beta,\ \gamma$) in the laboratory frame, are obtained from the dynamical expression [31]

$$\frac{\mathrm{d}\sigma^{(\hat{\boldsymbol{R}})}(\hat{\boldsymbol{r}}, t)}{\mathrm{d}\Omega_{\hat{\boldsymbol{r}}}} = \frac{8\pi\hbar^2}{mA_0^2}\, r^2 \left|\Psi^{(1)}(\boldsymbol{r}, t)\right|^2 \tag{15}$$

where $\Psi^{(1)}(\boldsymbol{r}, t)$ is the time-dependent wave function of Eq. (3). Eq. (15) provides a cross section valid for electrons arriving at some finite distance $\boldsymbol{r}$ from the molecular site after a finite time interval ($t > 0$) has elapsed subsequent to switching on the external field. In the limits $t\to\infty$ and $\boldsymbol{r}_e\to\infty$, Eq. (15) recovers the familiar stationary-state expression [2,3]

$$\frac{\mathrm{d}\sigma^{(\hat{\boldsymbol{R}})}(\hat{\boldsymbol{r}}_e, t)}{\mathrm{d}\Omega_{\hat{\boldsymbol{r}}}} \to \frac{\mathrm{d}\sigma^{(\hat{\boldsymbol{R}})}(\hat{\boldsymbol{k}}_e)}{\mathrm{d}\Omega_{\hat{\boldsymbol{k}}_e}} = \frac{4\pi^2 e^2}{m^2 c\omega} \times \left|\langle \Phi_{\boldsymbol{k}_e}^{(-)}(\boldsymbol{r}) | \hat{\boldsymbol{\epsilon}}\cdot\hat{\boldsymbol{p}} | \Phi_g(\boldsymbol{r})\rangle\right|^2 \tag{16}$$

for a particular ionic channel, where $\hat{\boldsymbol{k}}_e = (\phi_e, \theta_e)$ is the laboratory-frame direction of the ejected electron, and $\Phi^{(-)}_{\boldsymbol{k}_e}(\boldsymbol{r})$ is the final continuum eigenstate for this channel quantized in the direction of the out-going electrons, which satisfies incoming-wave boundary conditions and is Dirac normalized on the energy scale. Eq. (16), which is obtained from Eq. (15) employing the wave function of Eq. (8) and setting $\hat{\boldsymbol{r}}_e = \hat{\boldsymbol{k}}_e$, indicates that results equivalent to the standard stationary-state development can be obtained from Eq. (15) and the time-dependent formalism of Section 2, avoiding construction of any of the continuum eigenfunctions required in explicit use of Eq. (16).

3.1. Molecules fixed in space

Cross sections for molecules fixed in space are conveniently obtained from Eq. (15) by expressing the wave function of Eqs. (3) and (8) in terms of center-of-mass, principal-axis electron coordinates in the body frame ($\boldsymbol{r}_b$) and associated irreducible-tensor solutions of the body-frame Schrödinger equation. In the general case of elliptically polarized photons with propagation vector $\boldsymbol{k}_p$ in the laboratory-frame x direction having arbitrary amplitudes and phases in the y $[\boldsymbol{A}_y(t) = \hat{\boldsymbol{j}} A_y \cos(\omega t + \phi_y)]$ and z $[\boldsymbol{A}_z(t) = \hat{\boldsymbol{k}} A_z \cos(\omega t + \phi_z)]$ directions, where $\hat{\boldsymbol{j}}$ and $\hat{\boldsymbol{k}}$ are unit vectors in the laboratory frame, the appropriate wave function is

$$\Psi^{(1)}_{ell}(\boldsymbol{r}, t) = \frac{e}{mc} \sum_{\lambda=-1}^{+1} \left\{ A_z e^{-i\phi_z} D^{(1)}_{\lambda,0}(\hat{\boldsymbol{R}}) + A_y \mathrm{e}^{-i\phi_y} \frac{i}{\sqrt{2}} \left(D^{(1)}_{\lambda,+1}(\hat{\boldsymbol{R}}) + D^{(1)}_{\lambda,-1}(\hat{\boldsymbol{R}}) \right) \right\} \Psi^{(1)}_{\lambda}(\boldsymbol{r}_b, t). \tag{17}$$

Here, $D^{(1)}_{\lambda,0}(\hat{\boldsymbol{R}})$ and $D^{(1)}_{\lambda,\pm1}(\hat{\boldsymbol{R}})$ are rotation matrices [43], and $\Psi^{(1)}_{\lambda}(\boldsymbol{r}_b, t)$ are solutions of the body-frame Schrödinger equations ($\lambda = 0, \pm 1$)

$$\left(\hat{H}^{(0)}(\boldsymbol{r}) - i\hbar \frac{\partial}{\partial t} \right) \Psi^{(1)}_{\lambda}(\boldsymbol{r}_b, t) + \hat{H}^{(1)}_{\lambda}(\boldsymbol{r}_b, t)\, \Phi_g(\boldsymbol{r}_b) \times \mathrm{e}^{-iE_g t/\hbar} = 0 \tag{18}$$

where

$$\hat{H}^{(1)}_{\lambda}(\boldsymbol{r}_b, t) = (4\pi/3)^{1/2}\, Y^{(\lambda)}_1(\boldsymbol{p}_b) \cos(\omega t) \tag{19}$$

are irreducible-tensor (harmonic polynomial) electromagnetic perturbation operators in the body-frame [43]. Solutions of Eq. (18) for particular ionic channels are obtained employing λ-prepared eigenstates of $\hat{H}^{(0)}(\boldsymbol{r})$ similar to those of Eq. (4), with the momentum operator appearing there replaced by the irreducible-tensor operators of Eq. (19).

Referring to the development of Eqs. (1)–(9), the wave functions of Eqs. (17) and (18) have the asymptotic ($\boldsymbol{r}_b \to \infty$, $t \to \infty$) forms

$$\Psi^{(1)}_{\lambda}(\boldsymbol{r}_b, t) \to \mu_{\lambda}(E)\, \hat{\Phi}^{(\lambda)}_E(\hat{\boldsymbol{k}}_b) \left(\frac{m\pi}{2\hbar^2 k_b} \right)^{1/2} \left(\frac{1}{r_b} \right) \times \mathrm{e}^{i\left\{ k_b r_b + \frac{e^2 m}{k_b \hbar^2} \ln(2k_b r_b) - Et/\hbar \right\}} \otimes \Phi^{(N-1)}_{\Gamma}(\boldsymbol{r}_{N-1}), \tag{20}$$

where $\hbar\boldsymbol{k}_b$ is the body-frame electron momentum, and $\Phi^{(N-1)}_{\Gamma}(\boldsymbol{r}_{N-1})$ is the parent-ion eigenfunction for the ionic channel of energy E_Γ. The body-frame angular amplitudes $\hat{\Phi}^{(\lambda)}_E(\hat{\boldsymbol{k}}_b)$ and corresponding moments $\mu_\lambda(E)$ are given formally by expressions similar to Eqs. (4) and (5) employing the operators of Eq. (19), although they are more conveniently obtained directly from the invariant subspace development of Eqs. (10)–(12).

In the two important cases of linear ($A_y = \phi_y = \phi_z = 0$) and circular ($A_y = A_z$, $\phi_y - \phi_z = \mp\pi/2$) polarization, the cross sections obtained from Eqs. (15)–(20) take the forms

$$\frac{\mathrm{d}\sigma^{(\hat{\boldsymbol{R}})}_{lin}(\hat{\boldsymbol{k}}_e)}{\mathrm{d}\Omega_{\hat{\boldsymbol{k}}_e}} = \frac{4\pi^2 e^2}{m^2 c\omega} \left| \sum_{\lambda=-1}^{+1} D^{(1)}_{\lambda,0}(\hat{\boldsymbol{R}})\, \mu_{\lambda}(E)\, \hat{\Phi}^{(\lambda)}_E(\hat{\boldsymbol{k}}_b) \right|^2 \tag{21}$$

and

$$\frac{\mathrm{d}\sigma^{(\hat{\boldsymbol{R}})}_{r/l}(\hat{\boldsymbol{k}}_e)}{\mathrm{d}\Omega_{\hat{\boldsymbol{k}}_e}} = \frac{4\pi^2 e^2}{m^2 c\omega} \left| \sum_{\lambda=-1}^{+1} \left\{ D^{(1)}_{\lambda,0}(\hat{\boldsymbol{R}}) \mp \frac{1}{\sqrt{2}} \left(D^{(1)}_{\lambda,+1}(\hat{\boldsymbol{R}}) + D^{(1)}_{\lambda,-1}(\hat{\boldsymbol{R}}) \right) \right\} \mu_{\lambda}(E)\, \hat{\Phi}^{(\lambda)}_E(\hat{\boldsymbol{k}}_b) \right|^2 \tag{22}$$

where the subscripts r/l in the last equation refer to right- and left-handed helicities of approaching photons, respectively. It is clear from Eqs. (17)–(22) that the three complex amplitudes $\hat{\Phi}^{(\lambda)}_E(\hat{\boldsymbol{k}}_b)$ ($\lambda = 0$,

± 1) and associated transition moments are sufficient to determine the angular distributions of photoejected electrons for any molecular orientation in cases of linear and circular polarization. In employing Eqs. (21) and (22), it is important to bear in mind that the Euler angles $\hat{\boldsymbol{R}}$ are specified in the laboratory frame, whereas the electron ejection angles $\hat{\boldsymbol{k}}_b$ are given in the molecular body-frame.

3.2. Applications to diatomic molecules

Although the general polyatomic case is not any more complicated, it is helpful to write out the predictions of Eqs. (21) and (22) in the case of diatomic molecules ($\hat{\boldsymbol{R}} \rightarrow \phi_R,\ \theta_R$), and to normalize the resulting expressions to unity when integrated over all (4π) angles of electron emission, to obtain angular distributions appropriate for comparison with measured values [6–16]. Writing the required λ-prepared angular emission amplitudes in the conventional forms ($\lambda = 0,\ \pm 1$)

$$\hat{\Phi}_E^{(\lambda)}(\hat{\boldsymbol{r}}_b) = (\mp 1)^{\lambda}\, \hat{\Theta}_E^{(|\lambda|)}(\theta_b)(2\pi)^{-1/2}\, \mathrm{e}^{i\lambda\phi_b} \tag{23}$$

where the $\hat{\Theta}_E^{(|\lambda|)}(\theta_b)$ are unity-normalized (complex) functions of the body-frame polar angle θ_b of the ejected electron, and ϕ_b is the corresponding body-frame azimuthal angle, Eqs. (21) and (22) become

$$\left\{\frac{\mathrm{d}\sigma_{\mathrm{lin}}^{(\phi_R,\theta_R)}(\hat{\boldsymbol{k}}_e)}{\mathrm{d}\Omega_{\hat{\boldsymbol{k}}_e}}\right\}_{\mathrm{norm}} = \frac{|\cos\theta_R \hat{\Theta}_E^{(0)}(\theta_b) - \sqrt{2}\rho(E)\sin\theta_R\cos\phi_b \hat{\Theta}_E^{(1)}(\theta_b)|^2}{2\pi(\cos^2\theta_R + 2\rho^2(E)\sin^2\theta_R)} \tag{24}$$

and

$$\left\{\frac{\mathrm{d}\sigma_{r/l}^{(\phi_R,\theta_R)}(\hat{\boldsymbol{k}}_e)}{\mathrm{d}\Omega_{\hat{\boldsymbol{k}}e}}\right\}_{\mathrm{norm}} = \{|(\cos\theta_R \pm i\sin\theta_R\sin\phi_R)\,\hat{\Theta}_E^{(0)}(\theta_b) - \sqrt{2}(\sin\theta_R\cos\theta_R \pm i(\cos\phi_R\sin\phi_b - \cos\theta_R\sin\phi_R\cos\phi_b))\,\rho(E)\,\hat{\Theta}_E^{(1)}(\theta_b)|^2\}/\{2\pi(\cos^2\theta_R + \sin^2\theta_R\sin^2\phi_R + 2\rho^2(E)(1 + \sin^2\theta_R\cos^2\theta_R))\}, \tag{25}$$

where $\rho(E) = \mu_1(E)/\mu_0(E)$ is the indicated ratio of body-frame transition moments for the channel of interest [44–46].

Writing the two complex angular amplitudes in the form $\hat{\Theta}_E^{(\lambda)}(\theta_b) = |\hat{\Theta}_E^{(\lambda)}(\theta_b)|\ \mathrm{e}^{i\Phi_E^{(\lambda)}(\theta_b)}$, where $|\hat{\Theta}_E^{(\lambda)}(\theta_b)|$ are real non-negative magnitudes and $\Phi_E^{(\lambda)}(\theta_b)$ are corresponding phases, Eqs. (24) and (25) reveal that $|\hat{\Theta}_E^{(0)}(\theta_b)|$, $|\hat{\Theta}_E^{(1)}(\theta_b)|$, and the relative phase $\Phi_E^{(1)}(\theta_b) - \Phi_E^{(0)}(\theta_b)$ are sufficient to determine cross sections for both linearly and circularly polarized monochromatic photons for arbitrary orientations of diatomic molecules in the laboratory frame. These three basic quantities can be calculated following the invariant subspace development described above, and compared with values inferred from experiment employing a variety of particular orientations and polarizations [6–16].

Measurements performed to date using linearly polarized photons have favored detection of ejected electrons in the so-called 'dipole' plane perpendicular to the photon propagation direction, and the use of polarization 'parallel' ($\phi_R = 0, \theta_R = 0$) and polarization 'perpendicular' ($\phi_R = \pi/2,\ \theta_R = \pi/2$) molecular configurations [6–16]. In these two arrangements, with $\phi_b = 0$ or π, Eq. (24) takes the forms

$$\left\{\frac{\mathrm{d}\sigma_{\mathrm{lin}}^{(0,0)}(\hat{\boldsymbol{k}}_e)}{\mathrm{d}\Omega_{\hat{\boldsymbol{k}}_e}}\right\}_{\mathrm{norm}} = |\hat{\Theta}_E^{(0)}(\theta_b)|^2;$$
$$\left\{\frac{\mathrm{d}\sigma_{\mathrm{lin}}^{(\pi/2,\pi/2)}(\hat{\boldsymbol{k}}_e;\hbar\omega)}{\mathrm{d}\Omega_{\hat{\boldsymbol{k}}_e}}\right\}_{\mathrm{norm}} = |\hat{\Theta}_{E_\omega}^{(1)}(\theta_b)|^2 \tag{26}$$

indicating that normalized measured angular distributions in these molecular configurations provide directly the magnitudes $|\hat{\Theta}_E^{(0)}(\theta_b)|$ and $|\hat{\Theta}_E^{(1)}(\theta_b)|$ appearing in Eqs. (24) and (25). Additional measurements made in the dipole plane employing linear polarization and the molecular configurations ($\phi_R = \pi/2,\ \theta_R$) are seen to provide information on the cross term $2\ \mathrm{Re}\{\hat{\Theta}_E^{(0)}(\theta_b)^*\hat{\Theta}_E^{(1)}(\theta_b)\} = 2|\hat{\Theta}_E^{(0)}(\theta_b)|\,|\hat{\Theta}_{E_\omega}^{(1)}(\theta_b)|\cos(\Phi_E^{(1)}(\theta_b) - \Phi_E^{(0)}(\theta_b))$ also appearing in Eq. (24). Specifically, the molecular configuration $\phi_R = \pi/2, \theta_R = \pi/4$ in Eq. (24) for linear polarization, with $\phi_b = 0$ or π, gives the expression

$$\left\{\frac{d\sigma_{lin}^{(\pi/2,\pi/4)}(\hat{\boldsymbol{k}}_e)}{d\Omega_{\hat{\boldsymbol{k}}_e}}\right\}_{norm} = \frac{|\hat{\Theta}_E^{(0)}(\theta_b) - \sqrt{2}\rho(E)\cos\phi_b\hat{\Theta}_E^{(1)}(\theta_b)|^2}{2\pi(1+2\rho^2(E))}, \quad (27)$$

which evidently provides $\cos(\Phi_E^{(1)}(\theta_b) - \Phi_E^{(0)}(\theta_b))$ when the other information $[|\hat{\Theta}_E^{(0)}(\theta_b)|, |\hat{\Theta}_E^{(1)}(\theta_b)|, \rho(E)]$ appearing there has been previously determined.

In the case of circular polarization employing the parallel ($\phi_R = 0, \theta_R = 0$) molecular configuration and electron detection in the dipole plane ($\phi_b = \pi/2$ or $3\pi/2$) [14,16], Eq. (25) takes the form

$$\left\{\frac{d\sigma_{r/l}^{(0,0)}(\hat{\boldsymbol{k}}_e)}{d\Omega_{\hat{\boldsymbol{k}}_e}}\right\}_{norm} = \frac{|\hat{\Theta}_E^{(0)}(\theta_b) \mp i\sqrt{2}\rho(E)\sin\phi_b\hat{\Theta}_E^{(1)}(\theta_b)|^2}{2\pi(1+2\rho^2(E))}. \quad (28)$$

Evidently, the sum of the right- and left-handed polarization distributions of Eq. (28)

$$\left\{\frac{d\sigma_r^{(0,0)}(\hat{\boldsymbol{k}}_e)}{d\Omega_{\hat{\boldsymbol{k}}_e}}\right\}_{norm} + \left\{\frac{d\sigma_l^{(0,0)}(\hat{\boldsymbol{k}}_e)}{d\Omega_{\hat{\boldsymbol{k}}_e}}\right\}_{norm} = \frac{|\hat{\Theta}_E^{(0)}(\theta_b)|^2 + 2\rho^2(E)|\hat{\Theta}_E^{(1)}(\theta_b)|^2}{\pi(1+2\rho^2(E))}, \quad (29)$$

can be employed to infer the value of the factor $\rho(E)$ in conjunction with the magnitudes $|\hat{\Theta}_E^{(0)}(\theta_b)|$ and $|\hat{\Theta}_E^{(1)}(\theta_b)|$ obtained from Eq. (26), whereas the difference

$$\left\{\frac{d\sigma_r^{(0,0)}(\hat{\boldsymbol{k}}_e)}{d\Omega_{\hat{\boldsymbol{k}}e}}\right\}_{norm} - \left\{\frac{d\sigma_l^{(0,0)}(\hat{\boldsymbol{k}}_e)}{d\Omega_{\hat{\boldsymbol{k}}_e}}\right\}_{norm} = \frac{\sqrt{2}\rho(E)\sin\phi_b}{\pi(1+2\rho^2(E))} 2Im\{\hat{\Theta}_E^{(0)}(\theta_b)^*\hat{\Theta}_E^{(1)}(\theta_b)\}, \quad (30)$$

can provide $\sin(\Phi_E^{(1)}(\theta_b) - \Phi_E^{(0)}(\theta_b))$.

Accordingly, measurements of electrons ejected in the dipole plane for the molecular configurations of Eqs. (26)–(30) are sufficient to determine the two real non-negative body-frame amplitudes, the relative phase factor and the parameter $\rho(E)$, which comprise the computational invariants of the ionization process in diatomic molecules. In practice, three molecular configurations are sufficient to determine the real amplitudes and relative phase, since there are always only two choices for the latter when either its sine or cosine are known, one of which gives unphysical results and can consequently be excluded from further consideration. Moreover, since $\cos(\Phi_E^{(1)}(\theta_b) - \Phi_E^{(0)}(\theta_b))$ is required in Eq. (24), and $\sin(\Phi_E^{(1)}(\theta_b) - \Phi_E^{(0)}(\theta_b))$ is required in Eq. (25), rather than the relative phase itself, the former values are sufficient in these cases to generate angular distributions for all possible diatomic molecular orientations and for all forms of linear or circularly polarized monochromatic photons. Accordingly, the development of Eqs. (23)–(30) shows that measurements performed employing only a very small subset of all possible combinations of molecular orientations and polarizations provide the aforementioned invariant molecular information, with additional measured data consequently rendered redundant through use of the present formalism.

3.3. Valence-shell $(4\sigma)^{-1}$ ionization of nitric oxide

As an illustrative example of the foregoing development, Fig. 3a shows the invariant amplitudes and relative phase extracted from linear and circular polarization measurements performed at $\hbar\omega = 40.8$ eV incident photon energy for 4σ ionization of NO molecules employing the molecular configurations of Eqs. (26)–(30) [16]. Note that the relative phase reported is placed in the interval 0 to 2π by convention, as it is of course determined only to within an arbitrary additive multiple of $\pm 2\pi$. The measured angular distributions of photoelectron intensities do not resolve the $c^3\Pi$ and $B^1\Pi$ ionic (NO^+) states produced upon 4σ orbital ionization [16], and accordingly refer to averages over the two channels [47]. The data points shown refer to values inferred directly from the measured calibrated intensities, whereas the dashed curves provide plausible smoothed representations of the experimental values. In the case of the amplitude $|\hat{\Theta}_E^{(1)}(\theta_b)|$, the smoothing curve was set to zero at the points $\theta_b = 0$ and π radians, in accordance with the a priori odd-parity symmetry requirement in this case. More elaborate processing of the measured data, which incorporates corrections due to finite instrumental angular aper-

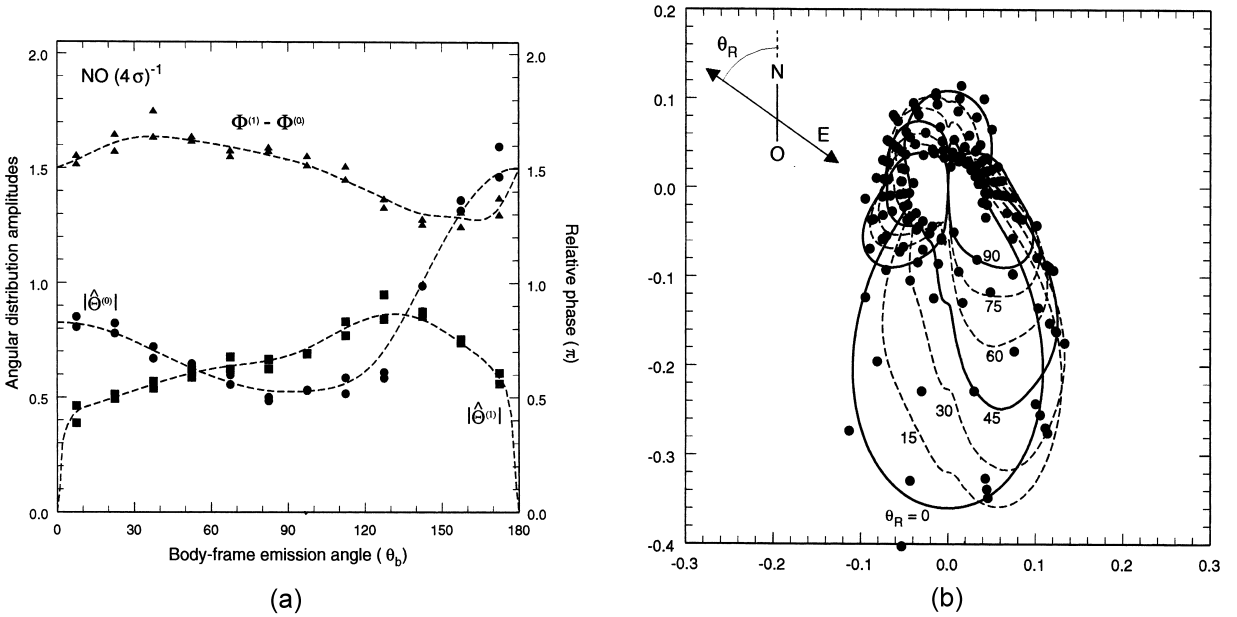

Fig. 3. (a) Invariant body-frame amplitudes and relative phase of Eqs. (24)–(30) for 4σ orbital ionization of NO molecules employing $\hbar\omega = 40.8$ eV photons [16]. The data points refer to values inferred from the appropriately calibrated measured angular distributions of photoelectron intensities [16], as discussed in the text, whereas the dashed lines provide plausible smoothed representations of the measured values. The effects of the finite kinetic-energy resolution and angular acceptance apertures employed, of the delayed axial recoil of the dissociating fragment ions, and appropriate experimental error bars are described separately [16]. The measurements do not resolve the $c^3\Pi$ and $B^1\Pi$ NO^+ ionic states and so refer to average values for these two channels [47,48]. The NO molecule is aligned along the z-axis in the body frame with the N atom on top ($\theta_b = 0$) and the O atom on bottom ($\theta_b = \pi$). (b) Normalized body-frame angular distributions for 4σ orbital ionization of NO molecules employing $\hbar\omega = 40.8$ eV linearly polarized photons, constructed employing the results of (a) and Eq. (24) in the text, in comparison with measured values [16]. The value $\rho(E = 40.8\ \text{eV}) = 0.94$ inferred from the measured data and Eq. (29) is in good accord with previous calculations [47]. The insert depicts the angle θ_R between the polarization vector and the fixed vertical molecular NO axis. Note that $\phi_b = 0$ in Eq. (24) for the values on the right side of the figure, whereas $\phi_b = \pi$ for the values on the left side, with θ_b varying from 0 (top) to π (bottom) in both cases. The small irregularities in some of the predicted curves for $\theta_b \approx \pi$ are artifacts of the fitting procedure employed in (a) and should be regarded as unphysical.

tures and kinetic-energy resolution, the effects of delayed axial recoil of the dissociating fragment ions, and gives appropriate error bars, is provided elsewhere [16]. Two sets of data points are shown in Fig. 3(a) because the measurements were performed for electron emission angles varying from the N-atom direction of the fixed-in-space NO molecular axis over 2π radians in the dipole plane, providing redundant information and a measure of the consistency of the experimental procedure. That is, since θ_b varies over the interval 0 to π radians (Fig. 3a), measurements performed at additional angles in the dipole plane past the direction of the O atom at π radians measured along the fixed NO axis refer to a change in ϕ_b from 0 to π radians, and to a retracing of the angle θ_b from π back to 0 radians.

In Fig. 3b are shown the normalized angular distributions of electrons photoejected in the dipole plane predicted by Eq. (24) for a range of molecular configurations ($\phi_R = \pi/2$, $\theta_R = 0$ to $\pi/2$) employing the amplitudes and phase of Fig. 3a, in comparison with the independently measured values [16]. The complex variation of the angular emission pattern as the orientation of the molecule varies with θ_R over the interval 0 to $\pi/2$ is largely reproduced by the predictions of Eq. (24) and the invariant information of Fig. 3a to within the relevant error bars of the experiment [16]. These variations are consequences

of changes in the values sin θ_R and cos θ_R only, with the invariant factors of Fig. 3a, of course, constant in the body-frame. That is, the amplitudes $|\hat{\Theta}_E^{(0)}(\theta_b)|^2$, $|\hat{\Theta}_{E_\omega}^{(1)}(\theta_b)|^2$, and the cross term $2\mathrm{Re}\{\hat{\Theta}_E^{(0)}(\theta_b)^*\hat{\Theta}_E^{(1)}(\theta_b)\}$ contribute in differing amounts depending upon the orientation angle θ_R, variations which are entirely geometrical in nature, and are unrelated to the body-frame dynamics of electron photoejection. More generally, the relevant geometrical factors are given by the rotation matrices appearing in Eqs. (21) and (22). The essential dynamics of the photoionization process in the present case is contained in the invariant amplitudes and relative phase of Fig. 3a, which pertain to body-frame information and are not dependent upon the geometrical aspects of the ionization process described by Eqs. (24)–(30). Notably, these three quantities, which have been extracted directly from a very small sub-set of all potential measurements, are sufficient to evaluate Eqs. (21) and (22) for any orientation of molecule in the laboratory frame.

Previously reported theoretical studies of molecular partial-channel photoionization cross sections employing multiplet-specific potentials aid in interpreting the angular patterns of electron emission given by the magnitudes $|\hat{\Theta}_E^{(0)}(\theta_b)|$ and $|\hat{\Theta}_{E_\omega}^{(1)}(\theta_b)|$ reported in Fig. 3a [47,48]. These variations are largely consequences of the spatial characteristics of the 4σ orbital in NO [47], which in the first approximation is an anti-bonding linear combination of an N atom 2s orbital and a significantly larger O atom 2s/2p hybrid orbital with its positive lobe pointing away from the N atom [i.e. $4\sigma = 2s_N - (2s/2p)_O \approx (2s/2p)_O$]. As a consequence, the ejected electrons for body-frame parallel polarization are largely (but not entirely) described by combinations of $2s_O \rightarrow kp_0$ and $2p_O \rightarrow ks$, kd_0 waves which interfere constructively in the O-atom direction and destructively in N-atom direction, accounting for the very large emission in the O direction along the NO molecular axis exhibited by the distorted cosine-like distribution $|\hat{\Theta}_E^{(0)}(\theta_b)|$ in Fig. 3a. Similarly, for perpendicular polarization in the body frame, the $2s_O \rightarrow kp_{\pm 1}$ and $2p_O \rightarrow kd_{\pm 1}$ waves, which interfere constructively in the O-atom direction and destructively in N-atom direction, account qualitatively for the distorted sine-like distribution exhibited by $|\hat{\Theta}_E^{(1)}(\theta_b)|$ in Fig. 3a.

The relative phase reported in Fig. 3(a) is seen to be only weakly sensitive to the angle θ_b, behavior also in accord with the predominantly atomic O nature of the 4σ orbital ionization process. Moreover, because *k*s waves can contribute to the $4\sigma \rightarrow k\sigma$ ionization component, but not to the $4\sigma \rightarrow k\pi$ component, the numerical values of the relative phase of Fig. 3a is largely a consequence of the difference between the numerically larger atomic O $2p_O \rightarrow ks$ phase shift and the smaller $2s_O \rightarrow kp$ and $2p_O \rightarrow kd$ phase shifts [3]. Of course, the modest ($\approx 15\%$) deviations from constancy in the relative phase shown in Fig. 3a are related to the subtle effects of the anisotropic molecular potential on the various partial-wave contributions to the $4\sigma \rightarrow k\sigma$ and $k\pi$ body-frame ionization components, effects which can be accounted for by detailed ab initio molecular calculations following the development of Eqs. (10)–(12) [47].

4. Discussion and concluding remarks

The explicitly time-dependent description of molecular photoionization reported here provides an alternative possibly more inciteful theoretical perspective on issues familiar from stationary-state considerations [2,3]. The temporal and spatial natures of the wave functions for photoexcitation and ionization reported are in accord with intuitive expectations, but also exhibit hybrid classical-quantal natures which apparently have not been studied in detail previously. In particular, the spatially extended coherent nature of the Bethe front for molecular photoionization, described for motion in central potentials in the early work of Bethe [28], is at odds with commonly held ‘packet’ notions of electron photoejection. In the case of anisotropic potentials of interest here, the concise description of the modulation of the outgoing Bethe waves by a unity-normalized complex emission amplitude provides a new basis for calculating photoionization cross sections differential in ejection angles for polyatomic molecules. Scattering eigenstates are avoided in favor of direct construction of an invariant subspace of prepared states which comprise the correct infinite linear combinations of degenerate eigenchannel func-

tions, and which can be obtained employing L^2 methods.

The cross-sectional expressions reported for fixed-in-space molecules and other atomic aggregates in an arbitrary ionizing field help to separate the geometrical aspects of the ionization process from the physically significant body-frame dynamics, which can generally be expressed in terms of three complex invariant body-frame emission amplitudes and associated transition moments. In the special case of diatomic molecules, only two real amplitudes and one relative phase are required at a given photon energy to specify differential cross sections for all possible molecular orientations in the presence of linearly or circularly polarized ionizing radiation. An explicit example of the use of the invariant body-frame information in generating differential cross sections in diatomic molecules demonstrates the importance of the analytical expressions provided for this purpose. The new expression for photoionization cross sections is seen to provide results that are equivalent to those obtained from standard methods employing scattering eigenstates, but it also provides additional possibilities for manipulating and interpreting measured cross sectional values in the absence of detailed quantum-mechanical calculations, as illustrated by the use of the analytical expressions of Eqs. (26)–(30) in the example reported.

Although not described explicitly here, expressions for so-called anisotropy factors appropriate for descriptions of the angular emission patterns obtained from photoionization of randomly oriented molecules are readily derived from the cross sections reported. In this way, it is shown that anisotropy factors can be expressed directly in terms of the measured fixed-in-space photoionization distributions, providing a connection between the two different types of experiments [42]. Similarly, measurements of body-frame polarization components of absorption cross sections, generally performed employing electron-ion coincidence techniques [44–46], provide the ratio of body-frame transition moments which also appears in the fixed-in-space cross sections presented here, establishing a connection between the two independently performed experiments. Electron spin-resolved photoionization cross sections for both fixed-in-space and randomly oriented molecules are also readily obtained from the basic expressions given in the text for comparisons with experiments. Finally, the new development provides a basis for theoretical studies of dynamical target relaxation, associated photoelectron-ion correlation, and other specifically time-dependent post-collision interaction phenomena. These and related theoretical issues are presently under study and will be the subjects of subsequent reports.

Acknowledgements

This paper is dedicated to Professor Chris Brion on the occasion of his 65th birthday. We gratefully acknowledge stimulating interactions with Professor Brion and his research group over a period spanning more than three decades. We also thank Dr O. Gessner and Dr R. Dörner and their collaborators for kindly providing experimental results prior to publication, and for very helpful communications in this connection, and D. Rolles for useful discussion. This work was supported in part by grants from the US Air Force Office of Scientific Research and COLIENCIAS of Colombia.

References

[1] A. Einstein, Ann. Phys. 17 (1905) 132.
[2] H.A. Bethe, E.E. Salpeter, Quantum Mechanics of One- and Two-Electron Atoms, Springer, Berlin, 1957.
[3] J. Berkowitz, Photoabsorption, Photoionization, and Photoelectron Spectroscopy, Academic Press, New York, 1979.
[4] K. Siegbahn, C. Nordling, A. Fahlman, R. Nordberg, K. Hamrin, J. Hedman, G. Johansson, T. Bergmark, S.-E. Karlsson, I. Lindgren, B. Lindgrin, ESCA—Atomic, Molecular and Solid State Structure Studied by Means of Electron Spectroscopy, Almquist and Wiksells, Uppsala, Sweden, 1967.
[5] A. Greiner, E. Moxon, A.L. Robinson, L. Tamura (Eds.), Advanced Light Source Activity Report 2000, LBNL-47783, April 2001, Lawrence Berkeley National Laboratory, UC, Berkeley, CA 94720.
[6] E. Shigemasa, J. Adachi, M. Oura, A. Yagishita, Phys. Rev. Lett. 74 (1995) 359.
[7] F. Heiser, O. Gessner, J. Viefhaus, K. Wieliczek, R. Hentges, U. Becker, Phys. Rev. Lett. 79 (1997) 2435.
[8] E. Shigemasa, J. Adachi, K. Soejima, N. Watanabe, A. Yagishita, N.A. Cherepkov, Phys. Rev. Lett. 80 (1998) 1622.
[9] E. Shigemasa, J. Electron Spectrosc. Relat. Phenom. 88–91 (1998) 9.

[10] O. Gessner, F. Heiser, N.A. Cherepkov, B. Zimmermann, U. Becker, J. Electron Spectrosc. Relat. Phenom. 101–103 (1999) 113.
[11] S. Motoki, J. Adachi, Y. Hikosaka, K. Ito, M. Sano, K. Soejima, A. Yagishita, G. Raseev, N.A. Cherepkov, J. Phys. B 33 (2000) 4193.
[12] A. Lafosse, M. Lebech, J.C. Brenot, P.M. Guyon, O. Jagutzki, L. Spielberger, M. Vervloet, J.C. Houver, D. Dowek, Phys. Rev. Lett. 84 (2000) 5987.
[13] A. Landers, Th. Weber, I. Ali, A. Cassimi, M. Hattass, O. Jagutzki, A. Nauert, T. Osipov, A. Staudte, M.H. Prior, H. Schmidt-Böcking, C.L. Cocke, R. Dörner, Phys. Rev. Lett. 87 (2001) 013002.
[14] T. Jahnke, Th. Weber, A.L. Landers, A. Knapp, S. Schössler, J. Nickles, S. Kammer, O. Jagutzki, L. Schmidt, A. Czasch, T. Osipov, E. Arenholz, A.T. Young, R. Díez Muiño, D. Rolles, F.J. García de Abajo, C.S. Fadley, M.A. Van Hove, S. Semenov, N.A. Cherepkov, J. Rösch, M.H. Prior, H. Schmidt-Böcking, C.L. Cocke, R. Dörner, Phys. Rev. Lett. (2001) in press.
[15] W. Weber, O. Jagutzki, M. Hattass, A. Staudte, A. Nauert, L. Schmidt, M.H. Prior, A.L. Landers, A. Bräuning-Demian, H. Bräuning, C.L. Cocke, T. Osipov, I. Ali, R. Díez Muiño, D. Rolles, F.J. García de Abajo, C.S. Fadley, M.A. Van Hove, A. Cassimi, H. Schmidt-Böcking, R. Dörner, J. Phys. B 34 (2001) 3669.
[16] O. Gessner, Y. Hikosaka, B. Zimmermann, A. Hempelmann, R.R. Lucchese, J.H.D. Eland, P.-M. Guyon, U. Becker, Phys. Rev. Lett. (2002) submitted.
[17] R. Dörner, V. Mergel, O. Jagutzki, L. Spielberger, J. Ullrich, R. Moshammer, H. Schmidt-Böcking, Phys. Rep. 330 (2000) 95.
[18] A.G. Suites, R.E. Continetti, Imaging Chemical Dynamics, ACS Symposium Series 770, American Chemical Society, Washington, DC, 2000.
[19] D. Dill, J. Chem. Phys. 65 (1976) 1130.
[20] J.W. Davenport, Phys. Rev. Lett. 36 (1976) 945.
[21] D. Dill, J. Siegel, J.L. Dehmer, J. Chem. Phys. 65 (1976) 3158.
[22] N.A. Cherepkov, Chem. Phys. Lett. 87 (1982) 344.
[23] R.L. Dubs, S.N. Dixit, V. McKoy, Phys. Rev. Lett. 54 (1985) 1249.
[24] N.A. Cherepkov, G. Raseev, J. Adachi, Y. Hikosaka, K. Ito, S. Motoki, M. Sano, K. Soejima, A. Yagishita, J. Phys. B 33 (2000) 4213.
[25] N.A. Cherepkov, S.K. Semenov, K. Ito, S. Motoki, Y. Yagishita, Phys. Rev. Lett. 84 (2000) 250.
[26] R. Díez Muiño, D. Rolles, F.J. García de Abajo, F. Starrost, W. Schattke, C.S. Fadley, M.A. Van Hove, J. Electron Spectrosc. Relat. Phenom. 114–116 (2001) 99.
[27] R. Díez Muiño, D. Rolles, F.J. García de Abajo, C.S. Fadley, M.A. Van Hove, Phys. Rev. Lett. (2002) in press.
[28] H. Bethe, Ann. Phys. 4 (1930) 433.
[29] G. Breit, H. Bethe, Phys. Rev. 93 (1954) 888.
[30] L.A.D. Siebbeles, J.M. Schins, W.J. van der Zande, J.A. Beswich, Chem. Phys. Lett. 187 (1991) 633.
[31] J.C. Arce, Quantum Spectra and Dynamics, PhD dissertation, Indiana University, Bloomington, IN, 1992.
[32] K.C. Kulander, Phys. Rev. A 38 (1988) 778.
[33] K.C. Kulander, E.J. Heller, J. Chem. Phys. 69 (1978) 2439.
[34] U. Fano, J.W. Cooper, Phys. Rev. A 137 (1965) 1364.
[35] M.R. Hermann, P.W. Langhoff, Phys. Rev. A 28 (1983) 1957.
[36] P.W. Langhoff, in: D.G. Truhlar (Ed.), IMA Volumes in Mathematics and Its Applications, Mathematical Frontiers in Computational Chemical Physics, Vol. 15, Springer, Berlin, 1988, pp. 135–185.
[37] T.J. Gil, C.L. Winstead, P.W. Langhoff, Comput. Phys. Commun. 53 (1989) 123.
[38] P.W. Langhoff, S.T. Epstein, M. Karplus, Rev. Mod. Phys. 44 (1972) 602.
[39] R.G. Newton, Scattering Theory of Waves and Particles, Springer, Berlin, 1982.
[40] R.F. Barrett, L.C. Biedenharn, M. Danos, P.P. Delsanto, W. Greiner, H.G. Washweiler, Rev. Mod. Phys. 45 (1973) 44.
[41] D. Loomba, S. Wallace, D. Dill, J.L. Dehmer, J. Chem. Phys. 75 (1981) 4546.
[42] P.W. Langhoff, J.C. Arce, J.A. Sheehy, O. Hemmers, H. Wang, P. Focke, I.A. Selin, D.W. Lindle, J. Electron Spectrosc. Relat. Phenom. 114–116 (2001) 23.
[43] A.R. Edmonds, Angular Momentum in Quantum Mechanics, Princeton University Press, Princeton, NJ, 1957.
[44] N. Satio, I.H. Suzubi, Phys. Rev Lett. 61 (1988) 2760.
[45] K. Lee, D.Y. Kim, C.I. Ma, D.A. Lapiano-Smith, D.M. Hanson, J. Chem. Phys. 93 (1990) 7936.
[46] E. Shigemasa, K. Ueda, Y. Sato, T. Sasaki, A. Yagishita, Phys. Rev. A 45 (1992) 2915.
[47] M.R. Hermann, C.W. Bauschlicher, W. Huo, S.R. Langhoff, P.W. Langhoff, Chem. Phys. 109 (1986) 1.
[48] J.W. Gallagher, C.E. Brion, J.A.R. Samson, P.W. Langhoff, J. Phys. Chem. Ref. Data 17 (1988) 9.